SCIENCE CHINA Materials ARTICLES

mater.scichina.com link.springer.com

Published online 29 March 2018 | https://doi.org/10.1007/s40843-018-9241-x
Sci China Mater 2018, 61(9): 1209–1217

Enhanced thermoelectric performance of $Cu_{12}Sb_4S_{13-\delta}$ tetrahedrite *via* nickel doping

Fu-Hua Sun[1], Jinfeng Dong[1], Shaugath Dey[2], Asfandiyar[1], Chao-Feng Wu[1], Yu Pan[1], Huaichao Tang[1] and Jing-Feng Li[1,3*]

ABSTRACT **$Cu_{12}Sb_4S_{13}$ tetrahedrite has received great attention as an earth-abundant and environmental-friendly thermoelectric material. This work aims to uncover the thermoelectric performance-enhancing effect and the mechanism of nickel doping on tetrahedrite. A series of $Cu_{12-x}Ni_xSb_4S_{13-\delta}$ (x = 0.5, 0.7, 1.0, 1.5 and 2.0) compounds were synthesized by mechanical alloying combined with spark plasma sintering. It is found that the thermal conductivity sharply reduces with increasing Ni content over the entire temperature range, <0.9 W m^{-1} K^{-1}, accompanied with an enhanced thermoelectric power factor. The model predicted that the reduced lattice thermal conductivity is attributed to mid-frequency phonon scattering, caused by precipitates and dislocations resulting from Ni doping. Consequently, a high ZT value up to 0.95 at 723 K was achieved for $Cu_{11}NiSb_4S_{13-\delta}$, corresponding to a ~46% increase over non-doped $Cu_{12}Sb_4S_{13-\delta}$. Furthermore, the cyclic measurement showed that the Ni-doped tetrahedrites displayed high chemical stability.**

Keywords: nickel doping, tetrahedrite, thermoelectric

INTRODUCTION

Thermoelectric (TE) technologies for alternative and complementary power generators or refrigerators are heavily reliant upon the efficiency of converting heat to electricity [1,2]. The critical factor for assessing the efficiency is the dimensionless figure of merit defined as $ZT = S^2\sigma T/(\kappa_{electron} + \kappa_{lattice})$, where S is the Seebeck coefficient, σ is the electrical conductivity, $\kappa_{electron}$ and $\kappa_{lattice}$ are the electronic and lattice contributions to the thermal conductivity, and T is the absolute temperature, respectively. Various strategies have been proposed to optimize TE performance. Such strategies include maximizing the electrical transport property *via* the power factor (PF, $S^2\sigma$) while retaining desirable thermal conductivity or sharply reducing thermal conductivity whilst retaining relatively high PFs [3–6]. Subsequently, high ZT values have been successfully achieved, and increasing applications have been made in thermoelectric cooling devices and power generators. Great research progress has been especially achieved in Pb- and Te-based composites [7,8]. However, as these materials contain the toxic and expensive elements, the search for novel and environment-friendly Te- and Pb-free materials has drawn considerable attention in the thermoelectric community worldwide.

The ternary Cu-M-Q (M = Sb, Sn and Fe, and Q = S and Se, respectively) compounds, such as Cu_5FeS_4 [9], Cu_3SbS_4 [10] and Cu_2SnSe_3 [11], have attracted much attention, primarily due to their intrinsic low thermal conductivity, and the environment-friendly, cost effective nature. A canonical example here is $Cu_{12}Sb_4S_{13}$ tetrahedrite with cubic structure, broad band gap and abundant reserves [12,13].

As shown in Fig. 1, the crystal structure of $Cu_{12}Sb_4S_{13}$ is described using a complex unit cell. The Cu(1) atom forms a tetrahedron with four S(1) atoms, a Sb atom forms a triangular antiprism with three S(1) and three Cu(2) atoms, whilst the Cu(2) atom is bonded to one S(2) atom, two S(1) and two Sb atoms in a triangular bipyramid. Its single crystal X-ray diffraction (XRD) data [14] shows an increasing anharmonic displacement of the Cu(2) atom perpendicular to the direction of the S(2)-S(1) triangular plane with increasing temperature, which means that Cu(2) atoms tend to move towards higher coordination number. Neutralizing to copper atom expansion, the electrostatic repulsive interaction from Sb

[1] State Key Laboratory of New Ceramics and Fine Processing, School of Materials Science and Engineering, Tsinghua University, Beijing 100084, China
[2] School of Materials Science and Engineering, University of New South Wales, NSW 2052, Australia
[3] Advanced Materials Institute, Graduate School at Shenzhen, Tsinghua University, Shenzhen 518055, China
* Corresponding author (email: jingfeng@mail.tsinghua.edu.cn)

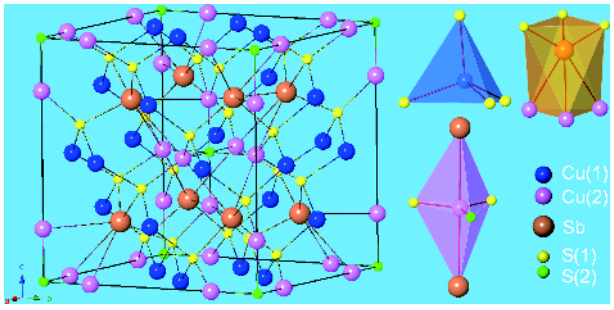

Figure 1 The crystal structure of $Cu_{12}Sb_4S_{13}$ is shown by the representative structure units: a CuS_4 tetrahedron with Cu(1) and S(1), a Sb[CuS_3]Sb trigonal bipyramid: S(1) and S(2) atoms around Cu(2) atom in the triangular plane; Sb atoms out of the plane, and a S_3SbCu_3 trigonal antiprism with Sb, S(1) and Cu(2) atoms.

atoms on both sides of the S(2)-S(1) plane is well enhanced, and then leading to a quasilocalized Cu(2) rattling mode. These rattlers can strongly couple acoustic phonons which are the main heat carriers, causing a low lattice thermal conductivity.

As for $Cu_{12}Sb_4S_{13}$ tetrahedrite, many chemical doping elements are available for reducing its thermal transport performance [15]. Although previous reports show Ni doping displays an effective role in $Cu_{12-x}M_xSb_4S_{13}$ (M = Mn, Fe, Co, Ni, Zn, G, etc.) [16–23], the effect of nickel in modifying the microstructure and enhancing thermoelectric performance has not been discussed in detail. Considering the limited solubility of Ni in the $Cu_{12}Sb_4S_{13}$ matrix, the secondary Ni-based phase accompanied by a precipitate of CuS appears at excessive Ni content. As a result, a strong extrinsic phonon scattering could be observed from these increased grain boundaries and introduced defects. Simultaneously, as to tetrahedrites, these precipitates can effectively improve its thermal stability [24]. However, their effect on lattice strain and electrical/thermal transport performance is not clear, which is the main focus of this study.

This study shows that $NiSb_2$ precipitates form when the nominal Ni content exceeds 0.7. According to the model prediction of lattice thermal conductivity, an effective scattering process for heat-carrying phonons resulted from the point defects, dislocations of secondary $NiSb_2$ and CuS phases at mid- and high-frequency phonons. A high and reversible TE property for $Cu_{12-x}Ni_xSb_4S_{13-\delta}$ was obtained by optimizing the Ni content. A maximal ZT value of 0.95 was achieved at 723 K for $Cu_{11}NiSb_4S_{13-\delta}$. This work comprehensively illustrates why Ni doping improves TE performance of $Cu_{12}Sb_4S_{13}$ materials, which is a critical step for clarifying the contribution of chemical modified $Cu_{12}Sb_4S_{13}$ tetrahedrites.

EXPERIMENTAL SECTION

Chemicals and samples preparation

All samples were synthesized by a powder metallurgical process combining mechanical alloying (MA) and spark plasma sintering (SPS). The experiments started from Sb shots (99.99%) and elemental powders of Cu (99.9%), Ni (99.9%) and S (99.99%), which were purchased from Aladdin Industrial Corporation (China). The raw materials were weighed in nominal compositions of $Cu_{12-x}Ni_xSb_4S_{12.7}$ (x = 0.5, 0.7, 1.0, 1.5 and 2.0) in a dry argon-filled glove box, loaded into a stainless steel vial and balls filled with gases of 95 vol% Ar and 5 vol% H_2, and subjected to MA at 450 rpm for 10 h in a planetary ball mill (QM-3SP2, Nanjing Nan Da Instrument Plant, China). The MA-derived powders were subsequently put into a 12 mm diameter graphite die, sintered into disks by SPS (SCM-1000-1, Fuji Electronic Industrial Co. LTD., Japan) at 723 K for 10 min in vacuum under an axial pressure of 50 MPa, and then cooled down to room temperature (RT) at a cooling rate of 15 K min^{-1}. A series of $Cu_{12-x}Ni_xSb_4S_{13-\delta}$ bulks with high relative densities (above 98%) were fabricated using this procedure.

Structural characterization

The phase identification of SPS $Cu_{12-x}Ni_xSb_4S_{13-\delta}$ samples was performed by XRD (D8 Advance diffractometer equipped with Ge (111) monochramator, Bruker, Germany) with Cu Kα radiation. The data were collected at 4° min^{-1} over an angular range from 15° to 65° with a step increment of 0.02°. The elemental valence and distribution of the surface-polished bulks were observed by X-ray photoelectron spectroscopy (XPS, Escalab 250Xi, Thermo Scientific, UK) with Al Kα radiation and electronic probe microscopic analysis (EPMA, JXA-8230, JEOL, Japan) with wavelength-dispersive spectrometer (WDS), respectively. The crystal structure and morphology were carried out by scanning/transmission electron microscopy (S/TEM, 2100F, JEOL, Japan) operated at 200 kV. The specific heat capacity (C_p) were investigated by differential scanning calorimetry (DSC, STA449, Netsch, Germany) with a heating rate of 10 K min^{-1} loaded into the closed-aluminum crucibles under an argon flow from RT to 723 K.

Thermoelectric transport property

The bar- and disk-shaped samples were cut and polished in preparation for the measurement of their thermoelectric properties. The electrical resistivity (ρ) and Seebeck coefficient (S) of bar-shaped bulks were measured

simultaneously using a Seebeck coefficient/electrical resistance measuring system (ZEM-2, Ulvac-Riko, Japan) at temperatures from 323 to 723 K under partial helium pressure. The thermal diffusivity (D) measured as a function of temperature was conducted using the laser flash model (TC-9000, Ulvac-Riko, Japan). Finally, the thermal conductivity (κ) was calculated by an equation of $\kappa = D\rho C_p$, in which ρ is the density measured by the Archimedes method. As temperature cooled down to RT, all samples (x = 0.5, 1.0, 1.5 and 2.0) were not taken out and measured again. The uncertainty of each TE parameter was estimated as 6% for Seebeck coefficient, 7% for electrical resistivity, +7.5%/−15% for power factor, 5–10% for thermal conductivity, and finally leading to a ~20% uncertainty for ZT value.

RESULTS AND DISCUSSION

Fig. 2 shows the thermoelectric properties of $Cu_{12-x}Ni_xSb_4S_{13-\delta}$ (x = 0.5, 1.0, 1.5 and 2.0) samples synthesized by a MA+SPS process. It should be noted that the data for the undoped sample (x = 0) are just for a reference, which should not be compared with the doped samples to figure out the compositional dependence since it was fabricated under a different condition in our previous study [25]. For all samples, the σ increased at first, peaked at ~623 K, and then decreased with increasing temperature. Fig. 2a also shows that increasing Ni content from x = 0.5 to 2.0 reduced the electrical transport properties, i.e., the σ values from 5.43 to 0.94 × 10^4 S m^{-1} at 723 K. However, the S values continuously increase with increasing temperature in Fig. 2b. The S values are largely enhanced with increasing Ni content, and the maximal value of 262 μV K^{-1} is obtained for x = 2.0 sample at 723 K. The reduced σ value along with the enhanced S indicates a possible decrease in the carrier concentration caused by Ni doping. Compared with the un-doped $Cu_{12}Sb_4S_{13-\delta}$ sample (x = 0) in our previous report [25], small Ni doping could significantly improve the electrical properties of tetrahedrite, as the σ value increased to 5.43 × 10^4 S m^{-1} for x = 0.5 compound at 723 K. However, excessive Ni content yields low σ and high S, suggesting the appearance of secondary phase, which will be discussed in detail later. Due to the improved S values, significantly higher power factors were obtained when compared to

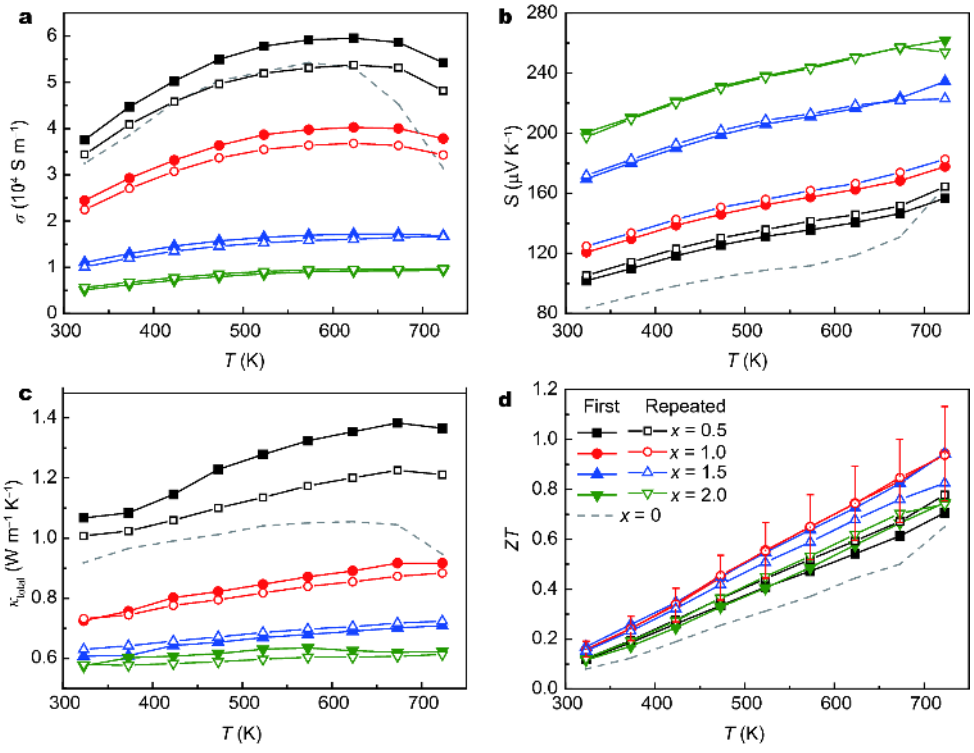

Figure 2 The temperature-dependence of (a) electrical conductivity, (b) Seebeck coefficient, (c) total thermal conductivity and (d) figure of merit ZT for the $Cu_{12-x}Ni_xSb_4S_{13-\delta}$ (x =0, 0.5, 1.0, 1.5 and 2.0) compounds synthesized by a MA+SPS method. The solid (labelled "first") and open (labelled "repeated") line-symbol lines indicate thermoelectric property measurement at the initial and cyclical testing for the same sample, respectively. Error bars in (d) represent 20% uncertainty in ZT values.

the $x = 0$ sample. As shown in Fig. S1, the highest value of 13.3 μW cm^{-1} K^{-2} was achieved for $Cu_{11.5}Ni_{0.5}Sb_4S_{13-\delta}$ at 723 K, an increase of ~56% over the un-doped sample.

As calculated from the measured C_p value in Fig. S2, the total thermal conductivity (κ_{total}) of $Cu_{12-x}Ni_xSb_4S_{13-\delta}$ is quite low. Fig. 2c shows a κ_{total} below 0.9 W m^{-1} K^{-1} over the temperature range from 323 to 723 K, except for the $x = 0.5$ sample. The κ_{total} values sharply decrease with increasing Ni content. The reduced thermal conductivity is due to the phonon scattering resulting from the complex crystal structures. Combined with the electrical performance and reduced thermal conductivity, the high thermoelectric performance was observed for $Cu_{12-x}Ni_xSb_4S_{13-\delta}$ from 323 to 723 K as shown in Fig. 2d. The highest ZT value of 0.95 was achieved at 723 K for the $x = 1.0$ composition, corresponding to ~46% enhancement as compared with the un-doped tetrahedrite. In this work, thermoelectric properties were cyclically measured in order to test the thermal stability and reversibility. As shown in Fig. 2, consistent performance was obtained for all Ni-doped $Cu_{12-x}Ni_xSb_4S_{13-\delta}$ samples over the entire temperatures, showing a < 8% reduction. Compared with the previously reported Ni-based tetrahedrites in Fig. S4, the $Cu_{11}NiSb_4S_{13-\delta}$ sample shows a higher ZT value at the optimal temperature.

As mentioned above, sharp changes in thermoelectric properties were observed when Ni content exceeded $x = 0.5$. The XRD patterns of the nominal composition $Cu_{12-x}Ni_xSb_4S_{12.7}$ ($x = 0.5$, 0.7, 1.0, 1.5 and 2.0) samples are shown in Fig. 3a. For the $x < 1.0$ samples, all peaks can be well indexed to the tetrahedrite phase (PDF#42-0561), indicating that they are single phase.

However, for the $x > 1.0$ samples, a new phase of $NiSb_2$ (PDF#25-1083) marked with asterisk sign (◆) appears and its intensity increases with increasing Ni concentration. From XRD refinement, an estimated 4.8 vol% $NiSb_2$ phase was obtained for the $x = 1.0$ sample in Fig. 3b. It is concluded that the solubility of Ni element in tetrahedrite matrix is less than 1.0 when using a MA+SPS process, and excessive Ni content would lead to the precipitate of $NiSb_2$ phase. To confirm the actual compositions of the $Cu_{12-x}Ni_xSb_4S_{12.7}$ samples, point analysis of the electroprobe microanalysis (EPMA) measurement was conducted. As listed in Table 1, it is clear that sulfur's stoichiometry within the samples shows a slight deviation from "13", so the actual compositions were defined as $Cu_{12-x}Ni_xSb_4S_{13-\delta}$ in this study.

To further confirm the chemical state of Ni element in the $Cu_{12-x}Ni_xSb_4S_{13-\delta}$ sample, XPS was carried out for the polished bulk surface (Fig. 4a shows its SEM image), and the results are presented in Fig. 4b. As found in the energy region of Ni for the $Cu_{11}NiSb_4S_{13-\delta}$ sample, the XPS spectra display two main asymmetric peaks with two satellites from Ni $2p_{3/2}$ and $2p_{1/2}$. The binding energy of Ni $2p_{3/2}$ satellite, 861.1 eV, is slightly lower than that of typical Ni^{3+} (861.4 eV), but significantly higher than that of Ni^{2+} (860.5 eV) [26]. Therefore, the average valence of Ni element is between +2 and +3. When Ni atoms enter Cu sites in $Cu_{12-x}Ni_xSb_4S_{13-\delta}$ compounds, more electrons are informed, and then carrier (hole) concentration decreases, which is well consistent with the results of electrical conductivity as shown in Fig. 2a. Fig. 4c–f show the

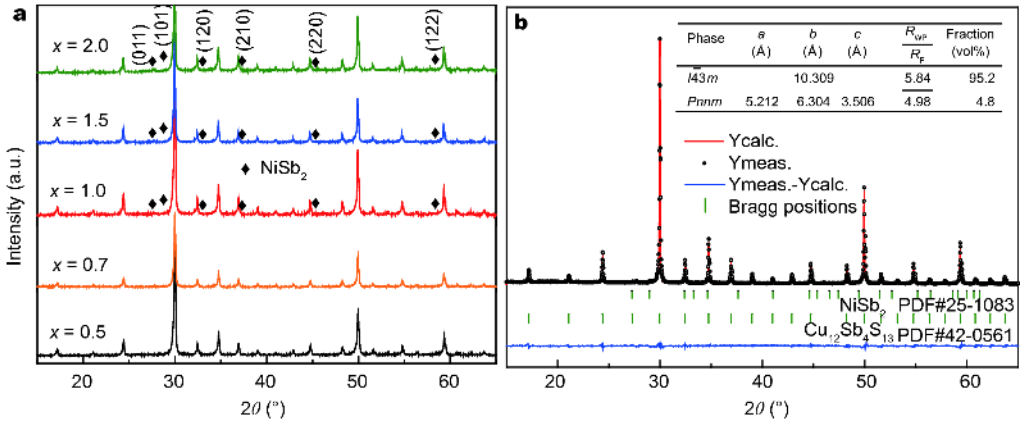

Figure 3 (a) XRD patterns of the SPSed $Cu_{12-x}Ni_xSb_4S_{13-\delta}$ ($x = 0.5$, 0.7, 1.0, 1.5 and 2.0) bulks at RT. The asterisk mask (◆) indicate diffraction peaks of $NiSb_2$. (b) Rietveld refinement of XRD pattern for $Cu_{11}NiSb_4S_{13-\delta}$ sample. XRD data collected over the range $15° \le 2\theta \le 65°$ for 1.5 s at each increment of 0.01°, the zero-point shift and asymmetry parameters of the diffraction peaks were systematically refined, and the background contribution was estimated using four polynomial functions. Lattice parameters, atomic coordinates, isotropic displacement parameters, site occupancies and phase volume fraction were finally varied to refine the crystal structure.

Table 1 Nominal and actual compositions for the $Cu_{12-x}Ni_xSb_4S_{12.7}$ (x = 0.5, 1.0, 1.5 and 2.0) compounds determined by EPMA measurement. The chemical formulae were averaged using point-analysis across five areas (in Table S1) and normalized to four antimony atoms per formula unit.

Nominal compositions	Actual compositions
$Cu_{11.5}Ni_{0.5}Sb_4S_{12.7}$	$Cu_{11.26}Ni_{0.50}Sb_4S_{12.19}$
$Cu_{11.0}Ni_{1.0}Sb_4S_{12.7}$	$Cu_{10.63}Ni_{0.99}Sb_4S_{12.45}$
$Cu_{10.5}Ni_{1.5}Sb_4S_{12.7}$	$Cu_{10.26}Ni_{1.40}Sb_4S_{12.58}$
$Cu_{10.0}Ni_{2.0}Sb_4S_{12.7}$	$Cu_{9.63}Ni_{1.89}Sb_4S_{12.56}$

EPMA element mapping of the polished $Cu_{11}NiSb_4S_{13-\delta}$ sample collected from the red rectangle in Fig. 4a, indicating that the Cu, Sb and S are homogeneously distributed. However, compared with the un-doped sample (Fig. S5), bright dots (indicated by white circles) appear in the Ni element map (Fig. 4f). These correspond to submicron sized Ni-based precipitates, which is well consistent with the XRD results in Fig. 3. Additionally, the second phase becomes more prominent at a higher Ni content (x = 2.0, as shown in Fig. S6).

Interestingly, the $NiSb_2$ precipitates were clearly observed and separated by CuS grain boundaries as shown by TEM in Fig. 5a. The STEM image in Fig. 5b also shows Ni and Sb enrichment along with a distinctive Cu–S boundary. As shown in Fig. 5a insert, a high resolution TEM (HRTEM) image free of defects in the (011) plane of $NiSb_2$ crystal was obtained along the [001] direction. However, from another zone axis of [111] direction as shown in Fig. 5c, the $NiSb_2$ precipitate is accompanied with amounts of dislocations, some of which are indicated a dashed circle in the figure. The selected area electron diffraction (SAED) in Fig. 5d displays a single crystal diffraction pattern, which corresponds well with two major growth orientations of $NiSb_2$ in (121) and (211). Fig. 5e is the HRTEM pattern taken from the CuS-$NiSb_2$ boundary, and presents a coherency between CuS and $NiSb_2$ with a fine orientation relationship of $(100)_{CuS}$ (a = 3.3410 Å) *via* $(011)_{NiSb2}$ (a = 3.2787 Å). The $NiSb_2$ phase reveals a relatively homogeneous contrast from [01−1] zone axis direction. This is confirmed by the diffraction pattern in Fig. 5g, except for some dark line-like features due to stacking defects, which is consistent with the dislocations in Fig. 5c. Fig. 5f shows a homogeneous Fourier transform pattern from the CuS grain boundary in [010] direction. We have also evaluated the density of the dislocations (D_0) with a square spacing of ~ 5 nm among the defects cores, which has an order of magnitude of 10^{-17} m^{-2}. Large quantity of vacancies (S vacancies in this study) would accelerate the formation of dislocation networks (as shown in Fig. 5c, e). This is consistent with the recent findings that the vacancy can activate and expand crystal dislocations in most of thermoelectric materials, especially selenides, which has been attracted much attention in the thermoelectric community [27–

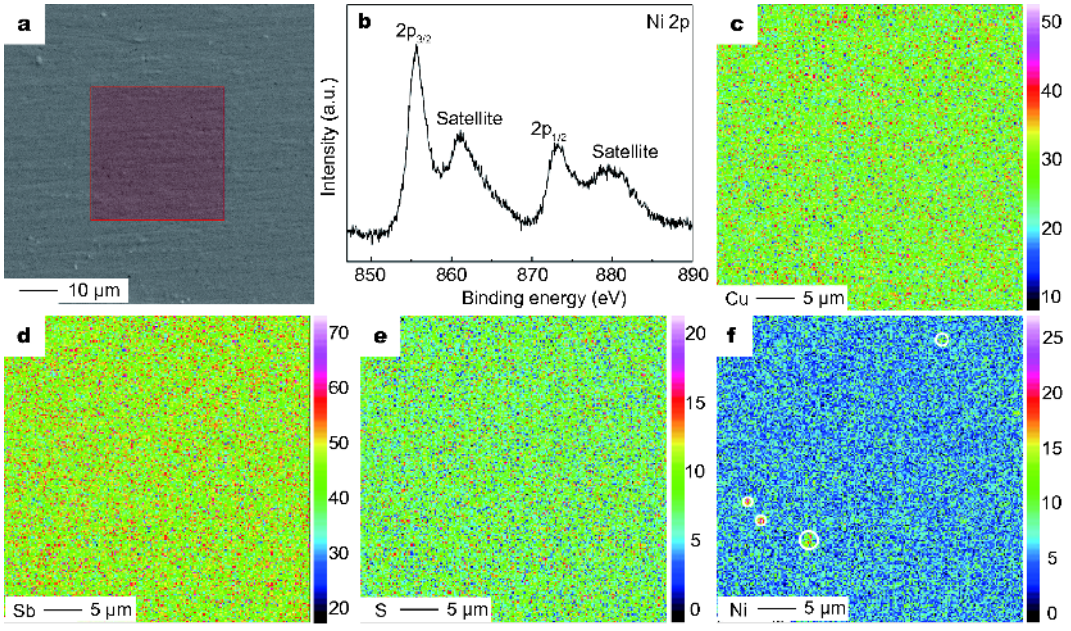

Figure 4 (a) SEM image and (b) XPS pattern for the polished surface of $Cu_{11}NiSb_4S_{13-\delta}$ sample, and the corresponding EPMA element maps of (c) Cu, (d) Sb, (e) S and (f) Ni taken from (a) marked in red square. The white solid circles indicate the precipitate of Ni-Sb phase.

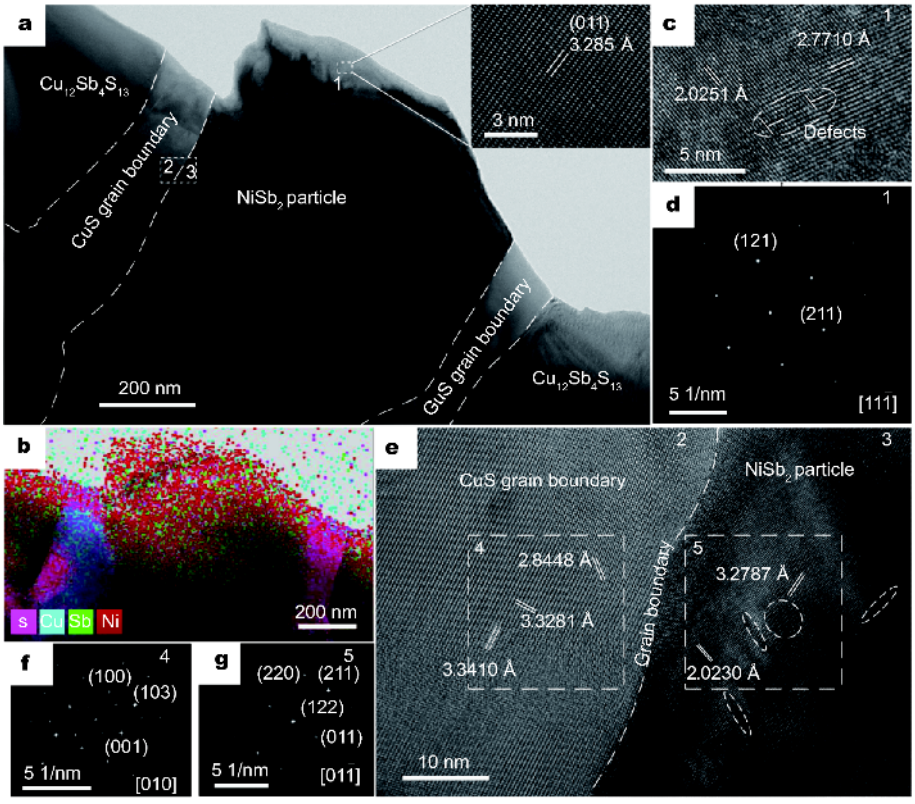

Figure 5 (a) Low-magnification bright-field image and (b) STEM mapping for $Cu_{11}NiSb_4S_{13-\delta}$ sample, clearly show the precipitate of $NiSb_2$ particle and CuS grain boundary. (c, e) HRTEM images taken from (a) marked numbers 1, 2 and 3. (d), (f) and (g) present the SAED and Fourier transform images corresponding to (a) and (e) labeled with 1, 4 and 5, respectively.

29].

In summary, Ni doping plays an important role in electrical-thermal transport and structural properties for thermoelectric tetrahedrites. Although Ni dopant acts as an effective donor, it partially enters the $Cu_{12}Sb_4S_{13}$ parent matrix and subsequently results in a precipitate of $NiSb_2$ and corresponding CuS grain boundary when its content exceeds 1.0. Further Ni addition would lead to the formation of defects, including point defects and dislocations. This significantly affects electrical transport and is also an important concern for thermal transport property (especially in lattice thermal conductivity) in the $Cu_{12-x}Ni_xSb_4S_{13-\delta}$ compounds.

In order to clarify the effect of $NiSb_2$ precipitates on thermal transport property, the $\kappa_{lattice}$ values were determined by subtracting the electric contribution *via* the Wiedemann-Franz law from the κ_{total} values. The Lorenz number (in Fig. S7) can be firstly obtained through an assumption of transport dominated by acoustic scattering and a single parabolic band combined with the reduced Fermi energy and measured Seebeck coefficient. The $\kappa_{lattice}$ values for x = 0.5 and 1.0 samples are shown in Fig. 6a. The phonon scattering depends on structure characteristics. Herein, we focused on the lattice thermal conductivity for x = 0.5 and x = 1.0 compositions because the x = 0 sample had a relatively low density due to the different processing conditions as mentioned above. Additionally, x = 0.5 composite is single phase, which can be used as a reasonable reference to clarify phonon scattering process. The $Cu_{11}NiSb_4S_{13-\delta}$ compound presents lower and reversible results at all temperatures in comparison with that of $Cu_{11.5}Ni_{0.5}Sb_4S_{13-\delta}$ tetrahedrite, and the lowest value reaches 0.46 W m^{-1} K^{-1} at 623 K.

To further ensure the effect of defects on reducing the thermal conductivity of $Cu_{12-x}Ni_xSb_4S_{13-\delta}$, modelling predication is carried out using the Debye-Callaway's equation [30]:

$$\kappa_{\text{lattice}} = \frac{k_B}{2\pi^2 v}\int_0^{\frac{k_B\theta_D}{\hbar}} \tau_C(\omega)\left(\frac{\hbar\omega}{k_BT}\right)^2 \frac{\omega^2 e^{\frac{\hbar\omega}{k_BT}}d\omega}{\left(e^{\frac{\hbar\omega}{k_BT}}-1\right)^2}. \quad (1)$$

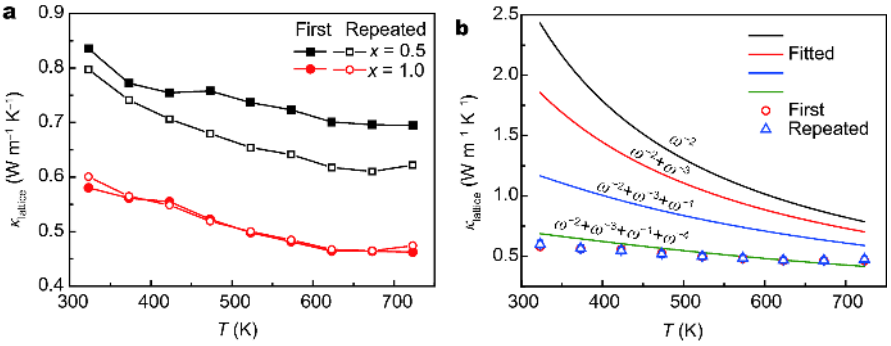

Figure 6 (a) The repeatedly measured lattice thermal conductivity as a function of temperature for x = 0.5 and 1.0 samples. (b) The theoretically calculated $\kappa_{lattice}$ values based on different models in comparison with experimental results for $Cu_{11}NiSb_4S_{13-\delta}$ sample.

In this equation, k_B is the Boltzmann constant, v is an average phonon-group velocity, θ_D is the Debye temperature which is obtained from the optimized value in heat capacity calculation, $\hbar$ is the reduced Plank constant, ω is the phonon angular frequency, and T is the absolute temperature, respectively. The lattice thermal conductivity can be expressed as a sum of phonon-scattering contributions with a relaxation time (τ_C) characterized by a frequency (ω) dependence in Equation (2) based on the XRD, EPMA and TEM observations.

$$\tau_C^{-1} = \tau_U^{-1} + \tau_N^{-1} + \tau_{DC}^{-1} + \tau_M^{-1} + \tau_{MF}^{-1}. \quad (2)$$

For polycrystalline $Cu_{12}Sb_4S_{13}$, a prominent open framework structure of $Sb[CuS_3]Sb$ containing loosely bonded Cu(2) rattlers is recognized as a mainly effective all-frequency phonon scattering factor, i.e., the Umklapp and normal processes [30] lead to a phonon-scattering behaved as $\tau_{U,N} \sim \omega^{-2}$. Additionally, the external dopants and composites are typically introduced to further reduce the $\kappa_{lattice}$ values in $Cu_{12}Sb_4S_{13}$ compounds. The corresponding phonon-scattering mechanisms are as follows [31,32]: the point defects or mass-fluctuation scattering with a relaxation time depending on frequency as $\tau_{PD/MF} \sim \omega^{-4}$ used for the high-frequency phonons end, and dislocation scattering targeting mid-range frequency phonons conducted as a relaxation time $\tau_{DC+DS+DE} \sim \omega^{-1}$ and ω^{-3}. For thermoelectric composites, the grain boundary contribution ($\tau_B \sim \omega^0$) plays an important role in phonon scattering at low-frequency end. However, in this study, considering that the sizes of CuS and $NiSb_2$ precipitated phases are relatively large for the calculation using the same relaxation time, the contributions for phonon scattering from CuS and $NiSb_2$ grain boundary were not taken into account in the calculation. More details for the modelling and parameters can be found in the Tables S2 and S3.

Therefore, we believe that introducing dopants and defects is an effective strategy to significantly reduce lattice thermal conductivity *via* phonon scattering. Firstly, the experimental $\kappa_{lattice}$ values are much lower than the black curve in Fig. 6b, as this model predicts that phonon-scattering only originates from the Umklapp and normal processes in a defect-free matrix. However, the predicted $\kappa_{lattice}$ sharply decreases if dislocation (red and blue solid curves) and mass-fluctuation scattering (green curve) contributions are included over the temperature range from 323 to 723 K. That is to say, the experimental $\kappa_{lattice}$ values of the $Cu_{11}NiSb_4S_{13-\delta}$ sample fit well with the $\omega^{-2} + \omega^{-3} + \omega^{-1} + \omega^{-4}$ model for both the initial and cyclic measurements. Based on the models in Fig. 6b and microstructure analysis, $NiSb_2$ precipitates are believed to cause the significant $\kappa_{lattice}$ reduction in $Cu_{12-x}Ni_xSb_4S_{13-\delta}$ tetrahedrites. Furthermore, these findings provide a comprehensive account that the mechanical strength (evidenced by repeatable thermoelectric properties) is significantly enhanced due to the existence of dense grain boundaries and defects [25].

CONCLUSIONS

The Ni-doped $Cu_{12-x}Ni_xSb_4S_{13-\delta}$ (x = 0.5, 1.0, 1.5 and 2.0) were synthesized using a simple MA+SPS method. Enhanced thermoelectric performance resulting from Ni doping was observed, and the highest ZT value of 0.95 was obtained for the $Cu_{11}NiSb_4S_{13-\delta}$ compound at 723 K. The thermal conductivity of the $Cu_{12-x}Ni_xSb_4S_{13-\delta}$ samples was significantly suppressed, accompanied by largely enhanced power factors with increasing Ni element content. It is found that the dislocations and special precipitates/inclusions associated with the $NiSb_2$ phase play a key role in enhancing the mid-frequency phonon scattering. The theoretical predictions of lattice thermal

conductivity are in good agreement with experimental results, indicating the importance of defects on the observed $\kappa_{lattice}$ reduction. The Ni-doped tetrahedrites show repeatable thermoelectric properties, suggesting a good thermal stability required for thermoelectric devices.

Received 3 February 2018; accepted 5 March 2018; published online 29 March 2018

1 Shakouri A. Recent developments in semiconductor thermoelectric physics and materials. Annu Rev Mater Res, 2011, 41: 399–431
2 Zhang QH, Huang XY, Bai SQ, *et al.* Thermoelectric devices for power generation: recent progress and future challenges . Adv Eng Mater, 2016, 18: 194–213
3 Li JF, Liu WS, Zhao LD, *et al.* High-performance nanostructured thermoelectric materials. NPG Asia Mater, 2010, 2: 152–158
4 Zhao LD, Tan G, Hao S, *et al.* Ultrahigh power factor and thermoelectric performance in hole-doped single-crystal SnSe. Science, 2016, 351: 141–144
5 Li JF, Pan Y, Wu CF, *et al.* Processing of advanced thermoelectric materials. Sci China Technol Sci, 2017, 60: 1347–1364
6 Li J. Unexpected boost of thermoelectric performance by magnetic nanoparticles. Sci China Mater, 2017, 60: 1023–1024
7 Liu W, Lukas KC, McEnaney K, *et al.* Studies on the Bi_2Te_3–Bi_2Se_3–Bi_2S_3 system for mid-temperature thermoelectric energy conversion. Energy Environ Sci, 2013, 6: 552–560
8 Pei Y, LaLonde A, Iwanaga S, *et al.* High thermoelectric figure of merit in heavy hole dominated PbTe. Energy Environ Sci, 2011, 4: 2085–2089
9 Qiu P, Zhang T, Qiu Y, *et al.* Sulfide bornite thermoelectric material: a natural mineral with ultralow thermal conductivity. Energy Environ Sci, 2014, 7: 4000–4006
10 Chen D, Zhao Y, Chen Y, *et al.* Thermoelectric enhancement of ternary copper chalcogenide nanocrystals by magnetic nickel doping. Adv Electron Mater, 2016, 2: 1500473
11 Liu G, Chen K, Li J, *et al.* Combustion synthesis of Cu_2SnSe_3 thermoelectric materials. J Eur Ceramic Soc, 2016, 36: 1407–1415
12 Vaqueiro P, Guélou G, Kaltzoglou A, *et al.* The influence of mobile copper ions on the glass-like thermal conductivity of copper-rich tetrahedrites. Chem Mater, 2017, 29: 4080–4090
13 Lu X, Morelli DT. Natural mineral tetrahedrite as a direct source of thermoelectric materials. Phys Chem Chem Phys, 2013, 15: 5762
14 Pfitzner A, Evain M, Petricek V. $Cu_{12}Sb_4S_{13}$: A temperature-dependent structure investigation. Acta Crystlogr B Struct Sci, 1997, 53: 337–345
15 Chetty R, Bali A, Mallik RC. Tetrahedrites as thermoelectric materials: an overview. J Mater Chem C, 2015, 3: 12364–12378
16 Suekuni K, Tsuruta K, Ariga T, *et al.* Thermoelectric properties of mineral tetrahedrites $Cu_{10}Tr_2Sb_4S_{13}$ with low thermal conductivity. Appl Phys Express, 2012, 5: 051201
17 Suekuni K, Tsuruta K, Kunii M, *et al.* High-performance thermoelectric mineral $Cu_{12-x}Ni_xSb_4S_{13}$ tetrahedrite. J Appl Phys, 2013, 113: 043712–043712
18 Heo J, Laurita G, Muir S, *et al.* Enhanced thermoelectric performance of synthetic tetrahedrites. Chem Mater, 2014, 26: 2047–2051
19 Suekuni K, Tomizawa Y, Ozaki T, *et al.* Systematic study of electronic and magnetic properties for $Cu_{12-x}TM_xSb_4S_{13}$ (TM = Mn, Fe, Co, Ni, and Zn) tetrahedrite. J Appl Phys, 2014, 115: 143702
20 Lu X, Morelli DT, Xia Y, *et al.* Increasing the thermoelectric figure of merit of tetrahedrites by co-doping with nickel and zinc. Chem Mater, 2015, 27: 408–413
21 Barbier T, Lemoine P, Gascoin S, *et al.* Structural stability of the synthetic thermoelectric ternary and nickel-substituted tetrahedrite phases. J Alloys Compd, 2015, 634: 253–262
22 Barbier T, Rollin-Martinet S, Lemoine P, *et al.* Thermoelectric materials: a new rapid synthesis process for nontoxic and high-performance tetrahedrite compounds. J Am Ceram Soc, 2016, 99: 51–56
23 Kosaka Y, Suekuni K, Hashikuni K, *et al.* Effects of Ge and Sn substitution on the metal–semiconductor transition and thermoelectric properties of $Cu_{12}Sb_4S_{13}$ tetrahedrite. Phys Chem Chem Phys, 2017, 19: 8874–8879
24 Bouyrie Y, Candolfi C, Ohorodniichuk V, *et al.* Crystal structure, electronic band structure and high-temperature thermoelectric properties of Te-substituted tetrahedrites $Cu_{12}Sb_{4-x}Te_xS_{13}$ ($0.5\leq x\leq 2.0$). J Mater Chem C, 2015, 3: 10476–10487
25 Sun FH, Wu CF, Li Z, *et al.* Powder metallurgically synthesized $Cu_{12}Sb_4S_{13}$ tetrahedrites: phase transition and high thermoelectricity. RSC Adv, 2017, 7: 18909–18916
26 Kalapsazova M, Stoyanova R, Zhecheva E, *et al.* Sodium deficient nickel–manganese oxides as intercalation electrodes in lithium ion batteries. J Mater Chem A, 2014, 2: 19383–19395
27 Lee Y, Lo SH, Chen C, *et al.* Contrasting role of antimony and bismuth dopants on the thermoelectric performance of lead selenide. Nat Commun, 2014, 5: 3640
28 Chen Z, Ge B, Li W, *et al.* Vacancy-induced dislocations within grains for high-performance PbSe thermoelectrics. Nat Commun, 2017, 8: 13828
29 Olvera AA, Moroz NA, Sahoo P, *et al.* Partial indium solubility induces chemical stability and colossal thermoelectric figure of merit in Cu_2Se. Energy Environ Sci, 2017, 10: 1668–1676
30 Callaway J, von Baeyer HC. Effect of point imperfections on lattice thermal conductivity. Phys Rev, 1960, 120: 1149–1154
31 Morelli DT, Heremans JP, Slack GA. Estimation of the isotope effect on the lattice thermal conductivity of group IV and group III-V semiconductors. Phys Rev B, 2002, 66: 195304
32 Zou J, Kotchetkov D, Balandin AA, *et al.* Thermal conductivity of GaN films: Effects of impurities and dislocations. J Appl Phys, 2002, 92: 2534–2539

Acknowledgements This work was supported by the Basic Science Center Project of National Natural Science Foundation of China (51788104 and 11474176), as well as Shenzhen Science and Technology Plan (JCYJ20150827165038323).

Author contributions Sun FH and Li JF designed the project; Sun FH, Dong J and Dey S performed the experiments and post-heat treatments; Sun FH wrote the paper with support from Li JF. All authors contributed to the general discussion.

Conflict of interest The authors declare no conflict of interest.

Supplementary information Supporting data are available in the online version of the paper.

Fu-Hua Sun is a PhD candidate at the School of Materials Science and Engineering, Tsinghua University. His current research focuses on the synthesis of nano-bulk composites and their applications in thermoelectrics.

Jinfeng Dong is a PhD candidate at the School of Materials Science and Engineering, Tsinghua University. His current research focuses on the synthesis of manganese-based materials and their applications in thermoelectrics.

Jing-Feng Li is a professor of Tsinghua University, China. He graduated from Huazhong University of Science and Technology (China) in 1984, and obtained his doctor degree from Tohoku University (Japan) in 1991. After working in Tohoku University as an assistant professor from 1992 to 1997 and an associate professor from 1997 to 2002, he joined Tsinghua University as full professor in 2002. His research interests include piezoelectric ceramics, composites and films for MEMS applications, thermoelectric materials and devices, materials microfabrication, ceramic processing and mechanical properties.

Ni掺杂提高$Cu_{12}Sb_4S_{13-\delta}$黝铜矿热电性能

孙富华[1], 董金峰[1], Shaugath Dey[2], Asfandiyar[1], 吴超峰[1], 潘瑜[1], 唐怀超[1], 李敬锋[1,3*]

摘要 $Cu_{12}Sb_4S_{13}$是一种储量丰富、环境友好的天然矿物, 被热电领域普遍关注. 本研究旨在揭示Ni掺杂提高黝铜矿材料热电性能的机理. 采用机械合金化(MA)结合放电等离子体烧结(SPS)的方法制备出$Cu_{12-x}Ni_xSb_4S_{13-\delta}$ (x = 0.5, 0.7, 1.0, 1.5, 2.0)样品. 实验结果表明, 在测量温度范围内(323–723 K), 随着Ni含量的增加, 样品的热导率急剧下降(< 0.9 W m^{-1} K^{-1}), 同时热电功率因子逐渐增加. 理论模型计算表明, 晶格热导率的降低主要来源于Ni掺杂引起的析出相及位错对中频声子的强散射作用. 由于较低的热导率和较高的功率因子, $Cu_{11}NiSb_4S_{13-\delta}$样品在723 K时获得最高$ZT$值0.95, 相对于未掺杂样品, 其热电性能提高了46%. 同时, 热循环测试表明, 通过Ni掺杂提高了黝铜矿热电材料的化学稳定性.

